Nuclear Science and Techniques (2026) 37:80
https://doi.org/10.1007/s41365-025-01873-3

Development and experimental validation of a symmetrical dual-chamber time projection chamber for high-precision neutron-induced fission cross-sectional measurement

Jia-Jun Zhang[1,2] · Jun Xiao[2] · Jing-Jing Xiao[1] · Jun-Jie Sun[2] · Tai-Ping Peng[2] · Pu Zheng[2]

Received: 14 February 2025 / Revised: 9 May 2025 / Accepted: 25 May 2025 / Published online: 11 February 2026

Abstract
Accurate fission cross-sectional data for actinide nuclides are critical for nuclear energy, astrophysics, and defense applications. Traditional detectors, such as fission chambers, face limitations in achieving sub-3% uncertainty owing to particle identification challenges and dynamic range constraints. The time projection chamber (TPC) can record both the energy deposition $\mathrm{d}E/\mathrm{d}x$ and the three-dimensional track of an event, providing the ability to identify particles and fission fragments. Based on this characteristic, we developed a novel TPC, INPC-TPC, featuring a symmetrical dual-chamber structure and gas electron multiplier (GEM)-based readout technology. The dual-chamber design isolates fission fragments and recoils protons, thereby reducing the dynamic range requirements of a single chamber, whereas the GEM ensures high spatial resolution and stable gain. Experiments conducted at the Chinese Spallation Neutron Source (CSNS) Back-n white neutron beamline validated the performance of the proposed detector. The INPC-TPC demonstrated effective fission fragment identification through particle energy-length correlation measurements and accurately measured the neutron beam spot size with a diameter relative error of $< 2\%$. The results highlight the capability of the system to achieve high-precision measurements of neutron-induced fission cross sections, particularly for ^{235}U and ^{238}U.

Keywords Time projection chamber · Fission cross section · Particle track reconstruction · Particle identification · Neutron beam spot

1 Introduction

With the widespread application of nuclear fission in new energy, national defense, astrophysics, and other fields, researchers have proposed higher requirements for the accuracy of fission cross-sectional data than before. Higher accuracy requirements have also driven the development of detectors. Traditional measurement methods, such as fission chambers, are limited by their own structure and measurement principles, and the accuracy of measuring the fission cross sections of major actinide nuclides is always between 3% and 5% [1]. Previous methods have struggled to achieve high levels of measurement accuracy. At present, the evaluation of fission cross sections based on a large number of experimental datasets can achieve a highly accurate level, and in some cases, can even reach an uncertainty of 1% [1]. However, in the fast neutron region (where the incident neutron energy ranges from 100 keV to 14 MeV), the measurement accuracy of the fission cross section for major fission nuclides such as ^{235}U and ^{238}U is usually between 3% and 5%. Higher requirements have been proposed for the measurement accuracy of fission cross sections in applications such as reactors, national defense, and nuclide synthesis calculations. Through extensive research on the impact of uncertainty, it has been concluded that a precision of 1% or higher is required [2]. In addition, as mentioned earlier,

This work was supported by the auspices of the Youth Doctoral Talent Incubation Program of the Second Affiliated Hospital of Army Medical University (No. 2024YQB060).

✉ Pu Zheng
1748650247@qq.com

[1] Bio-Med Informatics Research Center, Clinical Medical Research Center, Second Affiliated Hospital, Army Medical University, Chongqing 400037, China

[2] Institute of Nuclear Physics and Chemistry, China Academy of Engineering Physics, Mianyang 621000, China

the uncertainty of the system constrains the measurement accuracy. Consequently, to further enhance the measurement accuracy of fission cross sections, new measurement methods and detectors are urgently required.

The time projection chamber (TPC) was first proposed and invented by Nygren et al. in 1974 and was soon applied to PEP-4 experimental detection in the SLAC electron–positron collider [3]. TPC is a type of gas drift detector. It consists of drift areas of different shapes, readout detectors with positions (X-Y plane), and time measurement functions. The electron drift time can provide information in the Z-direction. A magnetic field can be applied parallel to the electric field to measure the momentum of the incident particles. Magnetic fields can also suppress transverse diffusion during electron drift, thereby improving the spatial resolution of the tracks. In contrast to other detectors, TPC detectors possess a sensitive volume that is sufficiently large to detect and reconstruct the three-dimensional track of the incident charged particles. It can record the energy deposition process of particles, thus measuring the ionization capacity $\mathrm{d}E/\mathrm{d}x$ of the particles [4, 5].

Based on these two characteristics, the TPC exhibits excellent performance in identifying particle types. Consequently, in numerous large-scale high-energy particle experiments, TPC has been used as central track detectors. Notable among these are ALEPH [6] and DELPHI [7] in LEP experiments, STAR [8] in BNL, and ALICE [9] in LHC. The European Organization for Nuclear Research (CERN) extensively deploys TPC detectors in experiments related to the Large Hadron Collider (LHC) [10]. In the ALICE experiment, TPC is responsible for detecting the massive charged particles generated in heavy-ion collisions. Researchers have combined advanced micro-pattern gas detectors (MPGDs) technology with TPC to achieve extremely high spatial resolution, reaching submillimeter levels.

The TPC detection technology has a very broad application prospect in the fission cross-sectional measurement. Traditional fission chambers record only the total energy deposited by fission events in the fission chambers. However, different types of particles, such as fission fragments, alpha particles, and protons scattered out of the target chamber, may generate events with similar energies, which leads to the inability of fission chambers to identify these types of particles. By incorporating the entire ionization process of charged particles within their effective volume, fission TPC can provide more effective particle identification capabilities. The fission TPC can record the deposited energy and length of the ionization tracks, which depend on the mass and charge of each particle. Heavy fission fragments lose energy rapidly, thus leaving shorter ionization tracks, whereas alpha particles have longer tracks. When the ionization tracks are plotted as a function of distance, there is a distinct peak (Bragg peak) in the ionization track of the alpha particles, indicating the maximum energy loss. By employing the ionization information of each particle, with the Bragg peak data included, the fission TPC can effectively identify the particle types.

The neutron-induced fission fragment tracking experiment (NIFFTE) collaboration is at the forefront of applying TPC to fission cross-sectional measurements [11, 12]. This fission TPC uses MICRO Mesh Gaseous Structure (MICROMEGAS) as the readout detector and has 5952 readout pads. It does not require a magnetic field to control diffusion because the drift distance is short (approximately 54 mm). The working gas was an argon-isobutane mixture at a pressure of 550 Torr. Recently, they measured the ^{239}Pu(n, f)/^{235}U(n, f) cross-sectional ratio (0.2–100 MeV) using this TPC, and the uncertainty of the results reached approximately 1%. They also used the NIFFTE TPC to measure the alpha/SF branching ratio of ^{252}Cf and obtained experimental results that were very close to the reference value [13].

A research team from Tsinghua University developed a time projection chamber prototype (fTPC) for conducting high-precision fission cross-sectional measurements [14]. They conducted discrimination experiments on fission fragments and alpha particles using a ^{252}Cf source, validated the fTPC's capability to distinguish between the two types of particles, and estimated the cross-sectional uncertainty introduced by the discrimination process in combination with simulation results. The fMeta-TPC, developed by Fudan University, focuses on low-energy nuclear experiments, such as cross-sectional measurements of photonuclear reactions [15]. This TPC employs a MICROMEGAS readout system. The experimental results demonstrate that this detector exhibits good energy and angular resolutions.

The Chinese Spallation Neutron Source (CSNS) team has also performed good work on fission TPC. One of the main purposes of the multipurpose TPC (MTPC) developed by the CSNS is to accurately measure the fission cross section [16–18]. The MTPC also uses MICROMEGAS as the readout detector, with a total of 1519 readout pads. The MTPC team has measured the cross section of ^{232}Th(n, f) at multiple energy points (4.50–5.40 MeV), and the results are consistent with the evaluation data [19, 20]. The relevant research team has also developed an open-source program framework called BLUET for simulation and data analysis based on MTPC, providing a convenient and efficient sharing platform for TPC data analysis by different research teams.

The INPC-TPC, independently developed by the Institute of Nuclear Physics and Chemistry of the Chinese Academy of Engineering Physics, is the third TPC detection system in the world specifically designed for neutron-induced cross-sectional measurements, following the NIFFTE TPC and MTPC. Its main purpose is to perform high-precision fission cross-sectional measurements (100 keV to 14 MeV) on actinide nuclides such as ^{235}U and ^{239}Pu, with the expectation of reducing the measurement uncertainty to 1% or less. To achieve such a high measurement accuracy, the selection of the reference cross section is crucial. As is known, most neutron-induced reaction cross sections are measured relative to the standard cross section, and few reaction cross sections can be directly measured. Therefore, the measurement accuracy of the fission cross section also depends to some extent on the accuracy of the standard cross section. At present, the fission cross-sectional measurements of commonly used actinide elements are usually based on the ^{235}U(n, f) cross section as the reference cross section for relative measurements; therefore, the uncertainty of the measurement results is difficult to reduce to a lower level. We designed the H(n, n) cross section as the reference cross section because the uncertainty of the H(n, n) cross section is currently the lowest among all standard cross sections (approximately 0.2%) [21]. This makes the goal we have set theoretically feasible. We completed the design and development of the entire system and conducted testing experiments on the white-light neutron source of the CSNS. The main body of the CSNS includes a 1.6 GeV fast-cycle proton synchrotron, an 80 MeV negative hydrogen linear accelerator, a central target station, and different neutron beam line pipelines [22–24]. After protons bombard the tungsten targets, some of the produced neutrons rebound. The CSNS separately leads to the neutrons flowing back along the target channel, creating a back-streaming white neutron beam (Back-n), which leads to two experimental terminals [25]. Back-n has the characteristics of high flight time resolution and high flux (up to 2×10^7 cm$^{-2}\cdot$s^{-1}), and has a wide energy range (0.5 eV to 200 MeV) and high-energy resolution.

This paper introduces the measurement principle and structural design of the INPC-TPC. As the third dedicated TPC worldwide for such measurements, following the NIFFTE and MTPC systems, the INPC-TPC introduces a pioneering symmetrical dual-chamber architecture and state-of-the-art gas electron multiplier (GEM)-based readout technology, addressing critical challenges in particle discrimination and dynamic range limitations. A defining feature of this design is the strategic use of the H(n, n) cross section as the reference cross section, leveraging its exceptionally low uncertainty to anchor absolute measurement precision. This choice, combined with the dual-chamber design that spatially isolates fission fragments and recoil protons to reduce single-chamber dynamic range requirements, and GEM's submillimeter spatial resolution and stable gain, establishes a robust framework for pushing the measurement uncertainty below 1%. By analyzing the experimental results obtained using back-n, it can be seen that INPC-TPC can effectively identify fission fragments and perform high-precision measurements on neutron beam spots.

2 Structure of the main chamber

The structure of the main chamber of the INPC-TPC is shown in Fig. 1. It mainly consists of a gas distribution system, field cage, gas electron multiplier (GEM), readout PCB, and preamplifier array. The detector housing was constructed from aluminum, providing sufficient mechanical strength and maintaining excellent gas tightness even when operating at 5 atm. Conversely, the metal housing serves as the detector's common ground while also providing electromagnetic shielding for the internal environment, thereby reducing noise in the readout signals. Both the housing body and end cover were tightly fastened to the readout PCB board, with silicone gaskets sealing all joints to ensure excellent gas tightness. Additionally, the housing features a hermetic high-voltage connector that maintains gas tightness while supplying a high voltage to the drift electrode. To enhance the uniformity of the electric field distribution within the TPC, the system is typically equipped with an electric field cage. The field cage consisted of two layers of copper rings arranged in a crossed pattern with equal spacing between adjacent rings. By applying a uniformly decreasing voltage across the copper rings, the uniformity of the electric field in the TPC was significantly improved. This uniformly decreasing electric field can be achieved through a series voltage division using identical resistors.

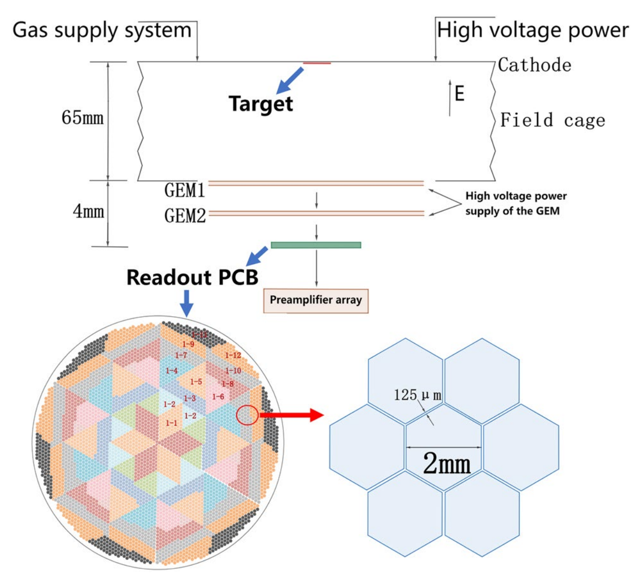

Fig. 1 (Color online) The structure of the main chamber and readout PCB

The INPC-TPC employs GEMs for the readout, in contrast to the NIFFTE and MTPC detectors, which utilize MICROMEGAS technology. GEMs demonstrate superior gain stability and reduced sparking risk owing to their cascaded amplification architecture, which distributes electric fields across multiple low-strength layers, mitigating localized charge accumulation [26, 27]. In contrast, MICROMEGAS relies on a single high-voltage gap, which concentrates the electric field and increases the discharge susceptibility under equivalent gain conditions. Studies further indicate the integrating GEM preamplification stages into MICROMEGAS systems significantly suppresses sparking rates [28, 29].

GEMs achieve enhanced spatial resolution via narrow electronic signal widths (~ 20 ns) and minimized lateral electron diffusion through multilayer hole compression [30]. A standard GEM consists of a 50–70 µm copper-clad polyimide foil, perforated with 30–50 µm diameter pores fabricated via photolithography and chemical etching techniques [31]. Voltages of hundreds of volts induce avalanche amplification within these microstructures. The INPC-TPC adopts GEM foils with 50 µm thickness, 70 µm pore diameter, and 140 µm pitch. To address the electric field non-uniformity at the foil edges, which is attributed to their smaller dimensions relative to the field cage components, guard rings are implemented alongside field cage supports, minimizing distortion and ensuring signal fidelity at high counting rates.

The particles generated by the target continuously ionize the working gas in a uniform electric field provided by the field cage, thus producing drift electrons. The GEM performs avalanche amplification on drifting electrons. Finally, the two-dimensional readout PCB collects electrons and provides signals with amplitude and time. The readout PCB (diameter 560 mm) consists of 4608 readout pads, as shown in Fig. 1. The size of the pad significantly affected the particle identification performance. During the early development process, we simulated the identification effects of four pad sizes: hexagons with diameters of 1, 2, 3, and 4 mm. The simulation results show that the smaller the pad size, the better the identification effect. However, when the pad size is too small, it also causes difficulties in engineering implementation. For a detailed analysis, please refer to reference [32]. After comprehensive consideration, we chose a pad diameter of 2 mm, with a spacing of 125 µm between each pad. Each pad was connected individually to a preamplifier, and a total of 4608 channels formed a preamplifier array. We can obtain the position information of the electron cluster in the X-Y plane based on the position of the pad that generates the signal. In addition, the position information of the electron cluster in the Z-direction can be determined by multiplying the drift time by the drift velocity. The drift velocity of the electrons was obtained through a Garfield++ simulation. Using the position distribution and signal amplitude of drift electrons in three-dimensional space, we can reconstruct the particle tracks and energy loss processes, thereby achieving particle identification. Previously, we used alpha particles emitted from the ^{241}Am source to measure the position resolution of the system. When the voltage of the GEM was 1300 V, the position resolution in the X-Y plane was 122 µm, which was obtained by performing Gaussian fitting on the residual distribution curve (σ = 122 µm) within the X-Y plane.

3 Design of the symmetrical dual-chamber structure

We use of the H(n, n) elastic scattering cross section as the reference cross section, and the calculation formula for the fission cross section is shown below:

$$\frac{\sigma_x}{\sigma_{\mathrm{H}}} = \frac{\epsilon_{\mathrm{H}}}{\epsilon_x} \cdot \frac{\Phi_{\mathrm{H}}}{\Phi_x} \cdot \frac{N_{\mathrm{H}}}{N_x} \cdot \frac{\sum_{\mathrm{XY}}(B_{\mathrm{H},i} \cdot n_{\mathrm{H},i})}{\sum_{\mathrm{XY}}(B_{x,i} \cdot n_{x,i})} \cdot \frac{\omega_x}{\omega_{\mathrm{H}}} \cdot \frac{C_x}{C_{\mathrm{H}}}, \tag{1}$$

where x is the nuclide to be measured, σ is the fission cross section, ϵ is the detection efficiency, Φ is the neutron flux. B_i and n_i represent the number of target nuclei and neutron flux at position i in discretized space, respectively. ω is the dead time correction coefficient, and C is the number of particles produced by the reaction. According to Eq. (1), the main physical parameters that we need to be measured include neutron flux and distribution Φ, the number and distribution of target nuclei B_i, and the number of reaction events C. The number of target nuclei can be calculated by measuring the spontaneous decay of alpha particles, as detailed in reference [33]. Owing to the significant differences in the energy loss among fission fragments, alpha particles, and recoil protons, there are certain variations in the settings of the electron gain values. If a single chamber is used to detect various particles, a larger dynamic range is required. Taking the ^{144}Ce source as an example, under 1 atm pressure, in P10 working gas (10% CH_4 + 90% Ar), the minimum energy loss is 3.4 keV/mm for 14 MeV protons, and the maximum energy loss is approximately 14 MeV/mm for 90 MeV ^{144}Ce fission fragments. The dynamic range between the two differed by approximately 4000 times. Therefore, we adopted a symmetrical dual-chamber structure to achieve separate measurements of protons and fission fragments, thus reducing the high requirements for the dynamic range of a single chamber. In this experiment, the electron gain value of Chamber 1 (for detecting fission fragments and alpha particles) was approximately 30. Because of the need to detect lower-energy recoil protons, Chamber 2 requires a higher gain value. The dual-chamber structure and internal configuration of the main chamber are shown in Fig. 2.

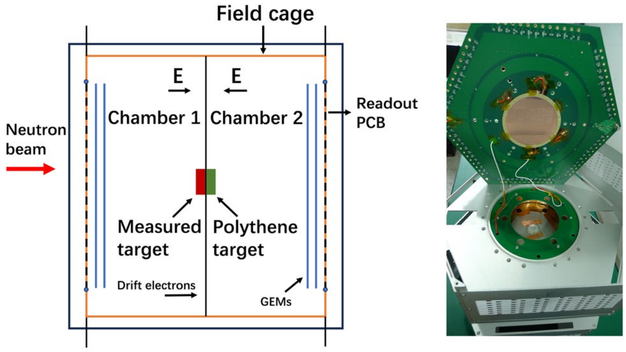

Fig. 2 (Color online) The structure of the dual-chamber system (left) and the main chamber (right)

The two chambers are filled with working gas, and the target to be measured (such as ^{235}U) is placed on the cathode plate in Chamber 1. Then, we placed the reference target (such as polyethylene) in a position corresponding to the target to be measured in Chamber 2. The neutron beam enters Chamber 1 and hits the target, producing fission fragments and alpha particles. Polyethylene targets serve as radiating bodies for neutron measurements. After hitting the target, the neutrons undergo elastic collisions with hydrogen atoms, resulting in the emission of recoil protons. The neutron flux on the target can be calculated based on the number of recoil protons. The fission cross-sectional ratio can then be calculated based on the elastic scattering cross section of hydrogen, the number of fission events, and the number of target nuclei.

4 Target and electronics systems

We used a partitioned target composed of ^{235}U and ^{238}U for fission cross-sectional measurement experiments, as shown in Fig. 3a, to achieve simultaneous measurement of ^{235}U and ^{238}U. The substrate of the target was 80 μm thick aluminum with a diameter of approximately 32 mm. We used a full electroplating process to deposit multiple elements onto the same substrate. The entire target was divided into four regions, each with a quarter-circle shape and a radius of approximately 15 mm. The distance between the target area and the edge of the substrate was approximately 1 mm. ^{235}U and ^{238}U are deposited on the diagonal areas of the substrate, respectively. The thickness unevenness and purity of the target were 8% and 99.9%, respectively. Polyethylene will be deposited in the area corresponding to ^{235}U and ^{238}U on the back of the substrate, which will be prepared for measuring the recoil protons.

To cover the complete particle tracks, the INPC-TPC has 4608 readout pads in a single chamber, totaling over 9000 channels. This poses a significant challenge to the performance of electronic systems. After the detector signals undergo front-end amplification, they are sent to the ADC sampling circuit boards for real-time sampling, and the data are finally transmitted to the DAQ system via optical fibers. The front-end circuit board adopts multichannel ASICs to achieve charge-sensitive preamplification and signal filtering and shaping. We conducted performance testing on the ASIC preamplifier of the TPC detector in the early stage, and its noise level was approximately 0.15 fC/1 pC (noise voltage 0.3 mV), with a dynamic range of approximately 6000:1. After connecting the data acquisition circuit, the noise of the system was approximately 0.6 mV, and the dynamic range was approximately 3000:1. The power consumption is approximately 10 mW/Ch. The sampling frequency of the system was 50 MS/s with 14 sampling bits. We used an RVD circuit to ensure that the voltages inside each GEM, between GEMs, and between GEMs and the readout PCB were consistent [26]. The INPC-TPC collects electrons through the pad and convolves the distribution of electrons in the pad in the preamplifier to obtain the output waveform. This differs from the collection of induction signals in traditional fission chambers.

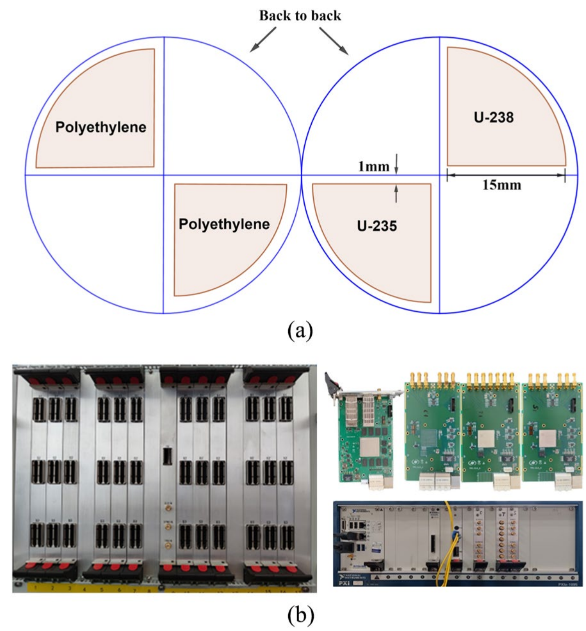

Fig. 3 (Color online) The structure of the partitioned target **a** and the electronics system **b**

The electronic system can be divided into two parts from a hardware perspective: the front-end data acquisition system and the back-end control and reception system [33], as shown in Fig. 3b. Front-end data acquisition uses a standard 6U chassis, and the data transmission card serves as the input of synchronous trigger signals and the output of data. Each data acquisition card contained 128 pairs of differential signal inputs. The data acquisition card communicates with the transmission card using a high-speed backplane to realize data exchange and command control. Furthermore, the data transmission card also receives and distributes external triggers, clock, and synchronization signals [33].

On the control side, we developed a data acquisition system control software based on LabVIEW. The software's functions include controlling the system's on/off, configuring parameters, monitoring the operating status of the chassis, selecting working modes, and more. We built a real-time data monitoring and display platform based on LabVIEW. Through this platform, we can also decode and segment the collected binary files into actual physical information, such as the channel number, arrival time, signal amplitude, and pulse width. The data acquisition system of the INPC-TPC stores the data of each chassis separately in the form of a binary file. The sampling frequency was one point per 20 ns. The content of the file is the waveform data after packaging and assembly, and each data packet contains 128 pieces of 16-bit data. When using the packaged data, ROOT software was used for decoding. We then used the TTree function in ROOT for data classification, storage, and retrieval.

5 White-light neutron source experiment

The main purpose of this neutron beam experiment was to test the fission fragment identification ability of the INPC-TPC; therefore, only Chamber 1 was installed, as shown in Fig. 4. The partition target was fixed on the PCB center hole at the connection between the two chambers using insulation tape. The layout of the experimental site is illustrated in Fig. 4. The neutron beam passes through different aperture neutron switches and collimator 1 and 2 to obtain beam spots of different sizes, which are then bombarded onto the target and ultimately captured by the neutron trap. We placed a 6 cm thick lead brick between the neutron switch and collimator 1 to reduce the beam intensity.

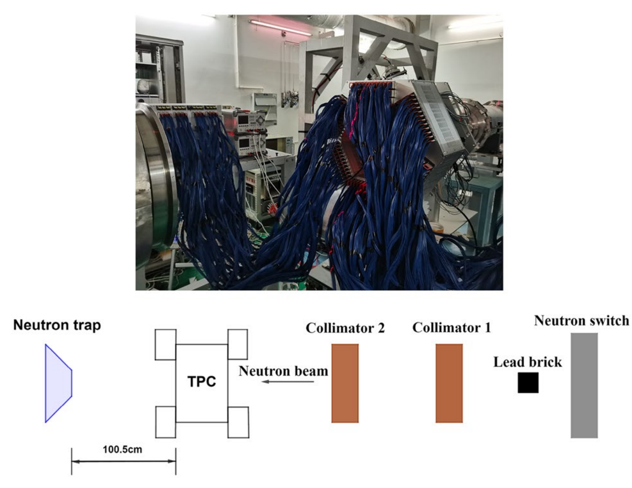

Fig. 4 The layout of the experimental site

The working gas used in the experiment was 90% Ar+10% CF_4. Electrons exhibit a high drift velocity in Ar (approximately 5 cm/μs), which reduces the signal time delay. With the addition of 10% CF_4, the diffusion coefficient of the gas mixture was lower, further reducing the lateral diffusion of the electron cloud during drift and thus enhancing the spatial resolution. The combination of Ar's low ionization energy (approximately 15.8 eV) and CF_4's electronegative properties enables the formation of a uniform electric field within the detector, optimizing electron transport paths and reducing signal distortion [34, 35]. The gas pressure was 100 kPa, and the flow rate was 50 SCCM. The cathode voltage was –2950V, GEM voltage was –1280V, and anode PCB voltage was 0 V. We used a resistor voltage divider circuit to ensure that the voltage across each gap was consistent (the voltage within the GEM, between GEMs, and between the GEM and the PCB was uniformly 320 V) in Chamber 1. The data collection threshold was 30 mV. The size of the neutron beam spot selected in the experiment was Φ30, corresponding to a neutron flux of approximately 6.1×10^5 cm^2/s. The proton pulse operation mode is a dual-beam cluster mode. The experiment was conducted in double-bunch mode. In the normal operation mode of the CSNS, two proton bunches with a time interval of 410 ns are present in each pulse, and the repetition frequency of the pulse is 25 Hz [36].

6 Processing methods for multitrack events

Owing to the wide energy range of white-light neutrons, some high-energy neutrons bombard the target, substrate, or GEMs, producing various types of particles. Therefore, in the white-light neutron mode, there may be more than one particle track in a single event. In the case where multiple particle tracks are superimposed in the same event, each track in the event must be separated and analyzed individually.

First, we reconstructed all tracks in all events. In this study, the reconstruction algorithm used was the 3D iterative Hough transform proposed by Dalitz et al. [37]. This algorithm uses spherical tessellation to discretize the parameter spaces. Compared with the direct discretization of the parameter space, this method can achieve better line-reconstruction results. The main steps for using this algorithm to perform line detection in point clouds are as follows:

1) Input point clouds $X = \{\vec{x}_1, ..., \vec{x}_n\}$;
2) Discretize all lines passing through the three-dimensional space of the point cloud in the parameter space;
3) Perform Hough transform on point cloud X;

4) Find the line parameter corresponding to the accumulator unit with the highest number of votes;
5) Count all the points whose distances to the line are less than the width of the cell (or the threshold);
6) Fit the optimal line using the orthogonal least square method;
7) Remove the points that have been used for least squares fitting from the accumulator;
8) Repeat steps 3 to 7 until either there are too few points within X or the predetermined number of lines has been found.

For the discretization of the parameter space, this algorithm adopts the tessellation of platonic solids proposed by Jeltsch et al. [38]. The number of vertices of a platonic solid is limited. The solid with the most vertices is an icosahedron, which has 12 vertices. If we inlay a point at the center between the vertices, we can obtain more vertices, and the discretized space will be more detailed. After multiple inlays, the polyhedron approaches a sphere, and at this time, the degree of discretization fineness is also the highest. However, it also requires higher computational memory and significantly reduces the computing speed. Therefore, an appropriate number of inlays must be selected to discretize the parameter space. In this experimental calculation, the number of inlays we adopt is 4.

One drawback of this reconstruction algorithm is that it treats all the input points as equivalent. However, in reality, the amplitude of each point is different, and particle tracks tend to be more biased toward points with larger amplitudes. Weight correction must be incorporated into the reconstruction algorithm. We used the signal amplitude of each point as a weight and used weighted least squares (WLS) to modify the Hough transform results [33].

After reconstruction, we obtained a line equation for each track. For a certain line L in the event,

$$L : \begin{bmatrix} x \\ y \\ z \end{bmatrix} = \begin{bmatrix} a_x \\ a_y \\ a_z \end{bmatrix} + t \begin{bmatrix} b_x \\ b_y \\ b_z \end{bmatrix}, \tag{2}$$

we use the following formula to calculate the distance between each point in the event and the line L,

$$d = \sqrt{\Delta x^2 + \Delta y^2 + \Delta z^2 - (\Delta x \cdot b_x + \Delta y \cdot b_y + \Delta z \cdot b_z)^2}, \tag{3}$$

$$\Delta x = a_x - x_0, \Delta y = a_y - y_0, \Delta z = a_z - z_0, \tag{4}$$

where d is the distance from a point to the line L, and (x_0, y_0, z_0) is the coordinate of the point. For points close to the line, their distance from the line is smaller than that of other points. Taking the first image in Fig. 5 as an example, we calculated the distance from each point to each line. Then, we set a threshold and considered points with a distance less than the threshold as points on the line. We used the diameter of two and a half pads as the distance threshold (5 mm). The reconstruction and splitting results of the tracks in an event are shown in Fig. 5. The coordinates of the Z-axis in the figure represent the relative positions.

After obtaining the linear equation for each track, we calculated the starting and ending positions of the track to calculate its length. In INPC-TPC, incident neutrons interact with the target under test, generating particles that move from the cathode (within the target area) to the anode plate. As these particles travel, they continuously ionize the working gas and generate electrons. Electrons ionized at the point where the particles exit are the farthest from the anode plate, thus experiencing the longest drift time. Consequently, these electrons arrive at the readout PCB the latest possible time. This pattern was observed for most of the particles. The electronic cluster that reaches the readout plate at the latest (with the maximum arrival time) is the electron that was ionized from the particle at the beginning, and its corresponding coordinate is the starting point of the track. The opposite site is the endpoint of the track. We find the coordinates of the point with the maximum arrival time in the track and then draw a perpendicular line to the reconstructed line. The intersection point of the perpendicular and reconstructed lines is approximately considered the starting point of the track, which is the initial ionization position. The termination position of ionization can also be obtained using this method. With the coordinates of the starting and ending points of the track, the length of the track can be calculated.

7 Detection of fission fragments

After using the method in the previous section for track reconstruction and splitting, we obtained all the particle tracks in Chamber 1. We calculated the starting point, ending point, and length of each track based on the track line equation. "Starting point" represents the point closest to the target in the track, while "ending point" represents the point closest to the upper GEM. We summed the integral amplitude of all points in each track to obtain the energy (represented by the number of channels) of that track, and thereby drew a 2D statistical graph of energy and length, as shown in Fig. 6a. This result is similar to that measured by the NIFFTE TPC [39]. We can clearly identify the fission fragments from the graph. In Fig. 6a, "p" represents the proton that may originate from the reaction between the neutrons and the detector materials or GEMs. The track length of p^* is concentrated at approximately 70 mm, which is close to the length of our chamber. We speculate that some high-energy protons have longer tracks, even exceeding the length of the chamber, and are thus truncated. The X part may be

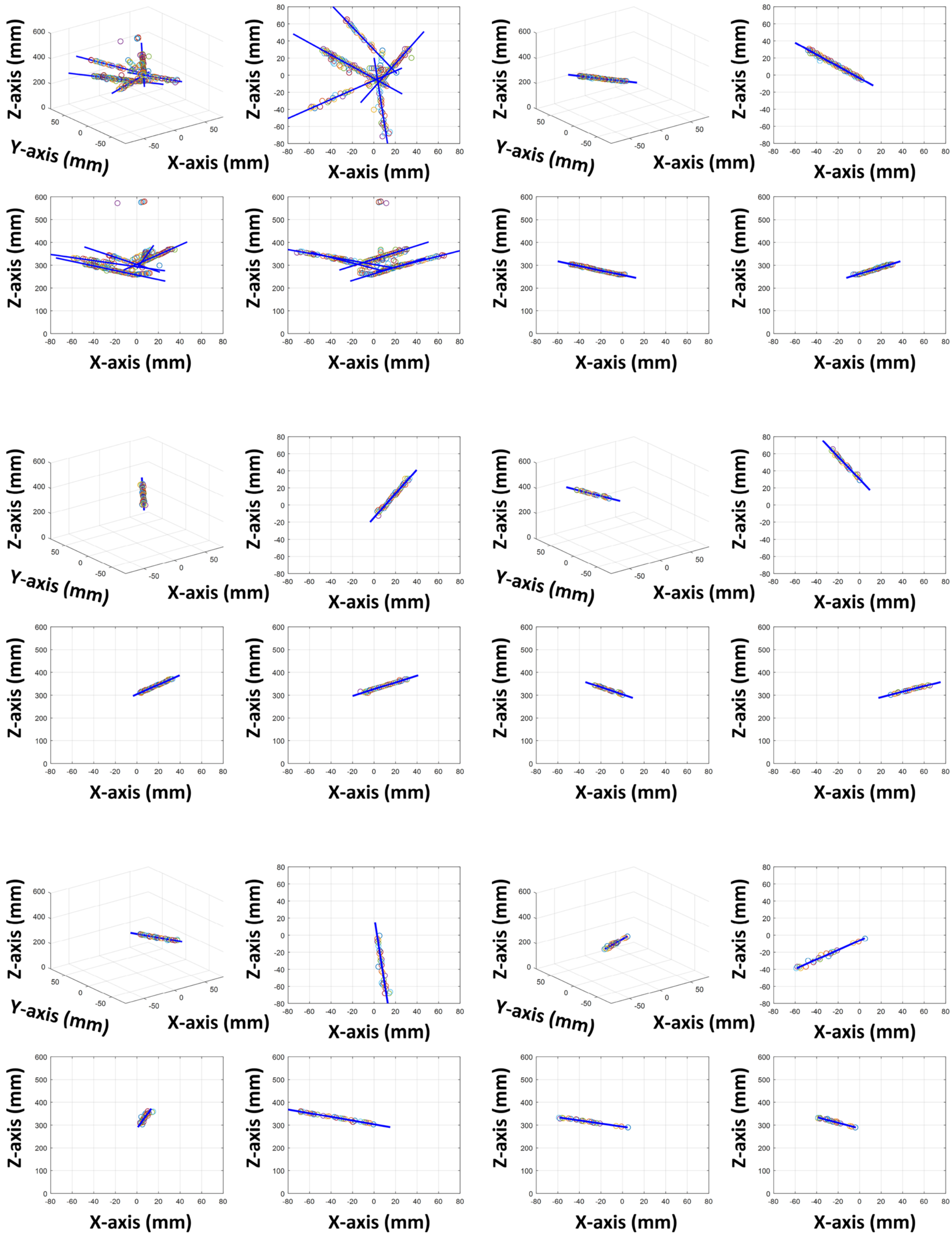

Fig. 5 (Color online) The result of track processing. The first image shows the original reconstruction result, and the following ones are the results after splitting. The circles in the figure represent the original points, and the blue lines represent the reconstructed lines

some lightweight charged particles, and we will conduct further experiments and analyze the specific components in the future.

We remove the part marked as frag in Fig. 6a and plotted the starting points of their tracks into a 2D distribution statistical map, as shown in Fig. 6b. The distribution of points in the figure precisely corresponds to the shape and position of the partitioned target, further confirming that this part is the fission fragments emitted from the target.

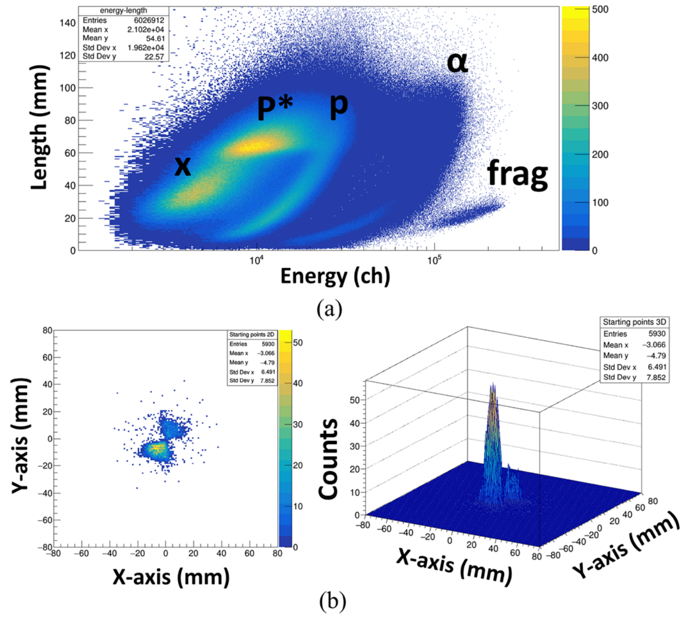

Fig. 6 (Color online) Measurement results: **a** the 2D statistical graph of energy and length; **b** the 2D distribution statistical map of the starting points (frag area)

8 Measurement of neutron beam spot

The large number of protons appearing in Chamber 1 was generated by collisions between neutrons hitting the GEM or readout PCB and the organic materials within them. These protons are emitted from the side near the GEM, and the 2D statistical distribution of their true track starting point, which is the "ending point" mentioned earlier, will be the shape of the neutron beam spot. By analyzing the 2D statistical distribution of the ending points of these tracks, the shape, size, and center position of the incident neutron beam spot can be calculated, as shown in Fig. 7a.

We projected the 2D distribution statistical map onto the X- and Y-axis, and performed Gaussian fitting on the statistical curve, as shown in Fig. 7b. By calculating the FWHM of the fitted curve, the diameter of the neutron beam spot was obtained as 30.52 mm (X-axis projection curve) and 29.43 mm (Y-axis projection curve). Compared with the standard diameter of 30 mm, the relative errors were 1.73% and 1.89%. The measurement accuracy was superior to that of the results measured by other research teams previously [40]. According to the fitting curve, the center position

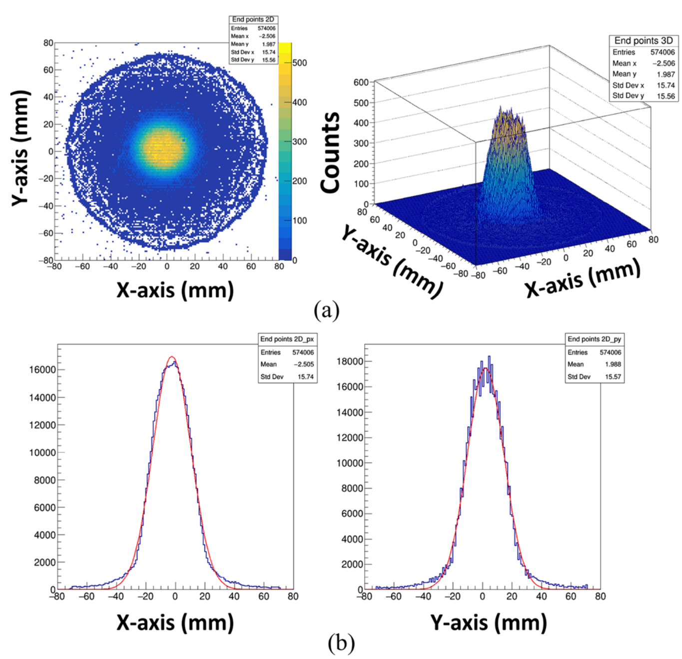

Fig. 7 (Color online) Measurement results of neutron beam spot: **a** the 2D and 3D distribution statistical map of the incident neutron beam spot; **b** the projection curve of the 2D distribution map toward the X-axis and Y-axis, where the red line represents the Gaussian fitting result

was calculated to be approximately (–2.52mm, 2.04 mm). Perhaps the placement of the detector was not accurately calibrated, resulting in a deviation from the center position.

9 Conclusion and outlook

This study introduces a new type of TPC detector, INPC-TPC, for fission cross-sectional measurements. Its core goal is to improve the accuracy of fission cross-sectional measurements for major actinide elements to 1% or higher. The characteristic of this TPC is the use of a larger readout detector and the clever design of a symmetrical dual-chamber structure, which enables the simultaneous measurement of protons and fragments. This study is an important test of the performance of the INPC-TPC. Within the wide energy range of white-light neutrons, we can still efficiently identify fission fragments, demonstrating the powerful particle identification ability of the INPC-TPC. In addition, we used this detector to measure the neutron beam spot, and the experimental results were very close to the reference values. Next, we will assemble Chamber 2 and conduct a neutron energy calibration experiment in the single-beam cluster mode. Another team will measure the number of target nuclei in the reference target. We expect that an accurate measurement of the cross-sectional ratio of ^{235}U(n,f)/H(n,n) and ^{238}U(n,f)/H(n,n) will be achieved.

Acknowledgements The author sincerely appreciates the experimental equipment and hardware support provided by the Institute of Nuclear Physics and Chemistry, Chinese Academy of Engineering Physics. The author also thanks the Chinese Spallation Neutron Source for providing the experimental conditions and technical support.

Author contributions All authors contributed to the study conception and design. Material preparation, data collection, and analysis were performed by Jun Xiao, Jun-Jie Sun, and Pu Zheng. The first draft of the manuscript was written by Jia-Jun Zhang, and all authors commented on previous versions of the manuscript. All authors read and approved the final manuscript.

Data availability The data that support the findings of this study are openly available in Science Data Bank at https://cstr.cn/31253.11.sciencedb.j00186.00796 and https://www.doi.org/10.57760/sciencedb.j00186.00796.

Declarations

Conflicts of Interest The authors declare that they have no conflict of interests.

References

1. M. Heffher, D.M. Asner, R.G. Baker et al., A time projection chamber for high accuracy and precision fission cross section measurements. Nucl. Instrum. Methods Phys. Res. Sect. A **759**, 50–64 (2014). https://doi.org/10.1016/j.nima.2014.05.057
2. G. Aliberti, G. Palmiotti, M. Salvatores et al., Nuclear data sensitivity, uncertainty and target accuracy assessment for future nuclear systems. Ann. Nucl. Energy **33**, 700–733 (2006). https://doi.org/10.1016/j.anucene.2006.02.003
3. D.R. Nygren, Origin and development of the TPC idea. Nucl. Instrum. Methods Phys. Res. Sect. A **907**, 22–30 (2018). https://doi.org/10.1016/j.nima.2018.07.015
4. T. Ohnuki, D.P. Snowden-Ifft, C.J. Martoff, Measurement of carbon disulfide anion diffusion in a TPC. Nucl. Instrum. Methods Phys. Res. Sect. A **463**, 142–148 (2001). https://doi.org/10.1016/S0168-9002(01)00222-4
5. V.C. Antochi, E. Baracchini, L. Benussi et al., Performance of an optically read out time projection chamber with ultra-relativistic electrons. Nucl. Instrum. Methods Phys. Res. Sect. A **999**, 165209 (2021). https://doi.org/10.1016/j.nima.2021.165209
6. T. Medcalf, M.R. Saich, J.A. Strong, A dedicated TPC track processor for the Aleph second level trigger. Nucl. Instrum. Methods Phys. Res. Sect. A **277**, 358–367 (1989). https://doi.org/10.1016/0168-9002(89)90764-X
7. C. Brand, R. Cirio, A. Foeth et al., Results on space measurement accuracy from tests of a half-scale DELPHI TPC prototype. Nucl. Instrum. Methods Phys. Res. Sect. A **252**, 413–417 (1988). https://doi.org/10.1016/0168-9002(86)91215-5
8. J.H. Thomas, A TPC for measuring high multiplicity events at RHIC. Nucl. Instrum. Methods Phys. Res. Sect. A **478**, 166–169 (2002). https://doi.org/10.1016/S0168-9002(01)01748-X
9. J. Baechler, T.C. Meyer, The ALICE time projection chamber-a technological challenge in LHC heavy ion physics. Nucl. Instrum. Methods Phys. Res. Sect. A **518**, 94–99 (2004). https://doi.org/10.1016/j.nima.2003.10.033
10. P. Gasik, For the ALICE collaboration. Building a large-area GEM-based readout chamber for the upgrade of the ALICE TPC. Nucl. Instrum. Methods Phys. Res. Sect. A **845**, 222–225 (2017). https://doi.org/10.1016/j.nima.2016.06.070
11. R.J. Casperson, D.M. Asner, J. Baker et al., Measurement of the normalized ^{238}U(n, f)/^{235}U(n, f) cross section ratio from threshold to 30 MeV with the NIFFTE fission Time Projection Chamber. Phys. Rev. C **97**, 034618 (2018). https://doi.org/10.1103/PhysRevC.97.034618
12. M. Monterial, K.T. Schmitt, C. Prokop et al., Measurement of material isotopics and atom number ratio with α-particle spectroscopy for a NIFFTE fission Time Projection Chamber actinide target. Nucl. Instrum. Methods Phys. Res. Sect. A **1021**, 165864 (2022). https://doi.org/10.1016/j.nima.2021.165864
13. L. Snyder, B. Manning, N.S. Bowden et al., Performance of a MICROMEGAS-based TPC in a high-energy neutron beam. Nucl. Instrum. Methods Phys. Res. Sect. A **881**, 1–8 (2018). https://doi.org/10.1016/j.nima.2017.10.028
14. Y. Yan, Y. Li, M. Huang et al., The differentiation between fission fragments and alpha particles by a time projection chamber. J. Instrum. **13**, P02014 (2018). https://doi.org/10.1088/1748-0221/13/02/P02014
15. H.K. Wu, X.Y. Wang, Y.M. Wang et al., Fudan multi-purpose active target time projection chamber (fMeta-TPC) for photonuclear reaction experiments. Nucl. Sci. Tech. **35**, 200 (2024). https://doi.org/10.1007/s41365-024-01576-1
16. W.H. Jia, Y. Lv, Z.Y. Zhang et al., Gap uniformity study of a resistive Micromegas for the Multi-purpose Time Projection Chamber (MTPC) at Back-n white neutron source. Nucl. Instrum. Methods Phys. Res. Sect. A **1039**, 167157 (2022). https://doi.org/10.1016/j.nima.2022.167157
17. Y.H. Chen, G.Y. Luan, J. Bao et al., Neutron energy spectrum measurement of the Back-n white neutron source at CSNS. Eur. Phys. J. A **55**, 115 (2019). https://doi.org/10.1140/epja/i2019-12808-1

18. R.R. Fan, Q. Li, J. Bao et al., Detector development at the Back-n white neutron source. Radiat. Detect. Technol. Meth. **7**, 171–191 (2023). https://doi.org/10.1007/s41605-022-00379-5
19. H.F. Bai, H. Yi, Y.K. Sun et al., Measurement of cross section for the ^{232}Th(n, f) reaction using a time projection chamber. Nucl. Instrum. Methods Phys. Res. Sect. A **1058**, 168912 (2024). https://doi.org/10.1016/j.nima.2023.168912
20. Z.Z. Ren, Y.W. Yang, K.J. Zhu et al., Measurement of the ^{232}Th (n, f) cross section in the 1–200 MeV range at the CSNS Back-n. Nucl. Sci. Tech. **34**, 115 (2023). https://doi.org/10.1007/s41365-023-01271-7
21. P. Marini, L. Mathieu, L. Acosta et al., Systematic investigation of background sources in neutron flux measurements with a proton-recoil silicon detector. Nucl. Instrum. Methods Phys. Res. Sect. A **841**, 56–64 (2017). https://doi.org/10.1016/j.nima.2016.10.026
22. J. Wei, H.S. Chen, Y.W. Chen et al., China spallation neutron source: design, R&D, and outlook. Nucl. Instrum. Methods Phys. Res. Sect. A **600**, 10–13 (2009). https://doi.org/10.1016/j.nima.2008.11.017
23. H.J. Wang, D.H. Zhu, L. Kang et al., The proton beam window for China Spallation Neutron Source. Nucl. Instrum. Methods Phys. Res. Sect. A **1042**, 167448 (2022). https://doi.org/10.1016/j.nima.2022.167448
24. H. Ouyang, H. Li, X. Cao et al., The operation and improvement of CSNS front end. Radiat. Detect. Technol. Methods **4**, 110–115 (2020). https://doi.org/10.1007/s41605-019-00159-8
25. J.Y. Tang, Q. An, J.B. Bai et al., Back-n white neutron source at CSNS and its applications. Nucl. Sci. Tech. **32**, 11 (2021). https://doi.org/10.1007/s41365-021-00846-6
26. J.J. Zhang, J. Xiao, J.J. Sun et al., Identification of α particles and fission fragments emitted by ^{252}Cf using a fission time projection chamber. Radiat. Meas. **174**, 107126 (2024). https://doi.org/10.1016/j.radmeas.2024.107126
27. S.N. Fan, B. Wang, H.R. Qi et al., Study on the performance of a high-gain gas electron multiplier-MicroMegas chamber. Acta Phys. Sin. **62**, 122901 (2013). https://doi.org/10.7498/aps.62.122901
28. D. Neyret, P. Abbon, M. Anfreville et al., Aging effects in the COMPASS hybrid GEM-Micromegas pixelized detectors. Nucl. Instrum. Methods Phys. Res. Sect. A **1065**, 169511 (2024). https://doi.org/10.1016/j.nima.2024.169511
29. P. Bhattacharya, S. Bhattacharya, N. Majumdar et al., Comparison of bulk micromegas with different amplification gaps. Nucl. Instrum. Methods Phys. Res. Sect. A **732**, 208–212 (2013). https://doi.org/10.1016/j.nima.2013.07.086
30. V.N. Kudryavtsev, T.V. Maltsev, L.I. Shekhtman, Spatial resolution of triple-GEM detectors. Nucl. Instrum. Methods Phys. Res. Sect. A **936**, 482–484 (2019). https://doi.org/10.1016/j.nima.2018.10.140
31. G. Bencivenni, G. Felici, F. Murtas et al., A triple GEM detector with pad readout for high rate charged particle triggering. Nucl. Instrum. Methods Phys. Res. Sect. A **488**, 493–502 (2002). https://doi.org/10.1016/S0168-9002(02)00515-6
32. Y.Y. Yan, Y.L. Li, M. Huang et al., The design of time projection chamber for fission cross-section measurements. In *2016 IEEE Nuclear Science Symposium, Medical Imaging Conference and Room-Temperature Semiconductor Detector Workshop (NSS/MIC/RTSD)*, Strasbourg, France, 2016, pp. 1–3. https://doi.org/10.1109/NSSMIC.2016.8069851
33. J.J. Zhang, J. Xiao, J.J. Sun et al., Determination of the number of ^{235}U target nuclei in the irregular target using a fission time projection chamber. Nucl. Eng. Technol. **56**, 444–450 (2024). https://doi.org/10.1016/j.net.2023.10.017
34. M. Peck, A. Göök, J. Enders et al., Pulse-height defect of Ar + CF_4 mixtures as a counting gas for fission-fragment detectors. Nucl. Instrum. Methods Phys. Res. Sect. A **919**, 105–112 (2019). https://doi.org/10.1016/j.nima.2018.12.060
35. T. Fujiwara, Y. Mitsuya, T. Yanagida et al., High-photon-yield scintillation detector with Ar/CF_4 and glass gas electron multiplier. Jpn. J. Appl. Phys. **55**, 106401 (2016). https://doi.org/10.7567/JJAP.55.106401
36. J. Wen, Y.W. Yang, Z.W. Wen et al., Measurement of the U-238/U-235 fission cross section ratio at CSNS – Back-n WNS. Ann. Nucl. Energy **140**, 107301 (2020). https://doi.org/10.1016/j.anucene.2019.107301
37. C. Dalitz, T. Schramke, M. Jeltsch, Iterative Hough transform for line detection in 3D point clouds. Image Process. Line **7**, 184–196 (2017). https://doi.org/10.5201/ipol.2017.208
38. M. Jeltsch, C. Dalitz, R. Pohle-Fröhlich, Hough parameter space regularisation for line detection in 3D. In *Proceedings of the 11th Joint Conference on Computer Vision, Imaging and Computer Graphics Theory and Applications–Volume 4: VISAPP*, Rome, Italy, 2016, pp. 345–352. https://doi.org/10.5220/0005679003450352
39. L. Snyder, M. Anastasiou, N.S. Bowden et al., Measurement of the ^{239}Pu(n, f)/^{235}U(n, f) cross-section ratio with the NIFFTE fission time projection chamber. Nucl. Data Sheets **178**, 1–40 (2021). https://doi.org/10.1016/j.nds.2021.11.001
40. C.C. Han, X.P. Ouyang, X.P. Zhang, Measurement of beam profile of CSNS Back-n. Atom. Energy Sci. Technol. **54**, 386–393 (2020). https://doi.org/10.7538/yzk.2019.youxian.0481